A Simple interpolation method for the carrier mobility in Trigate and gate-all-around silicon NWFETs from a non-equilibrium Green's Functions perspective

Zaiping Zeng, Francois Triozon, Yann-Michel Niquet, Sylvain Barraud

Quantum modelling of carrier mobility in Trigate and gate-all-around silicon NWFETs from a non-equilibrium Green's Functions perspective

Zaiping Zeng,[1,2] François Triozon,[3,2] Yann-Michel Niquet,[1,2,a)] and Sylvain Barraud[3,2]
[1)] *CEA, INAC-MEM, L_Sim, Grenoble, France*
[2)] *University Grenoble Alpes*
[3)] *CEA, LETI-MINATEC, Grenoble, France*

(Dated: 15 November 2016)

In the non-equilibrium Green's Functions (NEGF) framework, quantum calculations on the electron and hole mobilities have been performed on gate-all-around and Trigate rectangular silicon nanowire (SiNW) devices with leading dimension up to 50 nm. We find that when NW width or height falls in the sub-10 nm range, nearest neighbouring corner channels tend to merge and form "side channels" with much lower mobilities. The contribution from these "side channels" remains significant even at large effective channel width, causing a rather slow convergence towards the limit of thin film device. On top of these numerical results, a simple but effective interpolation model for the size-dependent modulation of carrier mobility in rectangular SiNW devices has been derived, which only requires the mobilities of square NW devices and of the limiting thin film devices as inputs. These mobilities can be obtained by combining contributions from partial mobilities limited by various common scattering mechanisms (phonons, surface roughness and remote Coulomb scattering). We provide these partial mobilities by NEGF calculations for reference devices with NW sizes or film thickness in sub-10 nm range. Empirical models for the carrier density dependent partial mobilities have been further developed. Finally, comparison with experimental data has been made to validate the derived mobility interpolation model and excellent agreement has been achieved.

I. INTRODUCTION

For the past two decades relentless focus on Moore's Law, transistor scaling has provided ever-increasing transistor performance and density[1,2]. Metal-Oxide-Semiconductor (MOS) transistors have evolved from classical, planar, single-gate devices to three-dimensional devices with a multi-gate structure [Double-Gate (DG), Trigate or Gate-All-Around (GAA) devices] in an effort to increase drive current and to control short-channel effects[3]. Among multi-gate architectures, Trigate and GAA silicon nanowire (SiNW) transistors demonstrate the best gate control and hence the best short-channel figures (sub-threshold slopes, drain-induced barrier lowering (DIBL), ...), being considered as promising candidates for next generation of electronic devices[3–6]. Carrier mobility is not only a significant concern as regarding device performance but also an essential characteristic for understanding transport phenomena. For SiNW systems, its behaviour has been studied both experimentally[7–12] and theoretically[13–25]. Many significant insights concerning structural confinement and carrier scattering effects have been provided. However, it remains unclear how the carrier mobility varies when going from SiNWs to silicon thin films. From modelling point of view, a facet dominated model proposed by Sekaric *et al.*[10] has been widely used to interpret the size-dependent modulation of carrier mobility in SiNWs devices. However, it requires the surface mobilities as inputs which are hardly accessible accurately, particularly for experiments. Furthermore, this model is based on decoupling of NW into four independent two dimensional planes. This practice very likely breaks down in ultra-thin NW devices where carrier conduction moves to the center of the device and all the facts are strongly correlated.

In this contribution, we compute the size-dependent carrier mobility modulation of both n-type and p-type rectangular Trigate and GAA silicon nanowire field effect transistors (NWFETs). Both [100] and [110] transport orientations are considered. The leading NW dimension varies from 7 nm up to 50 nm. We use a non-equilibrium Green's Functions (NEGF) approach, which explicitly accounts for quantum confinement effects and carrier scattering by phonons, surface roughness (SR) and remote Coulomb charges (RCS). Based on the numerical results, we have developed a simple but effective model which describes the size dependence of the carrier mobilities in rectangular SiNWs over a wide range of dimensions. It requires only the mobilities of thin film devices and of square NW devices as inputs, which can be easily obtained both theoretically and experimentally. The NEGF methodology as well as simulated devices will be introduced in the following section. In Section III, we present our calculated results and show how the simple mobility interpolation model is developed. We then validate this model by comparing with experimental data. The last section (Section IV) is devoted to conclusions.

II. DEVICES AND METHODOLOGY

The simulated devices are rectangular GAA and Trigate SiNW channels with width W and height H. For Trigate devices, the channel is etched in a (001) Silicon-

[a)] Electronic mail: yniquet@cea.fr

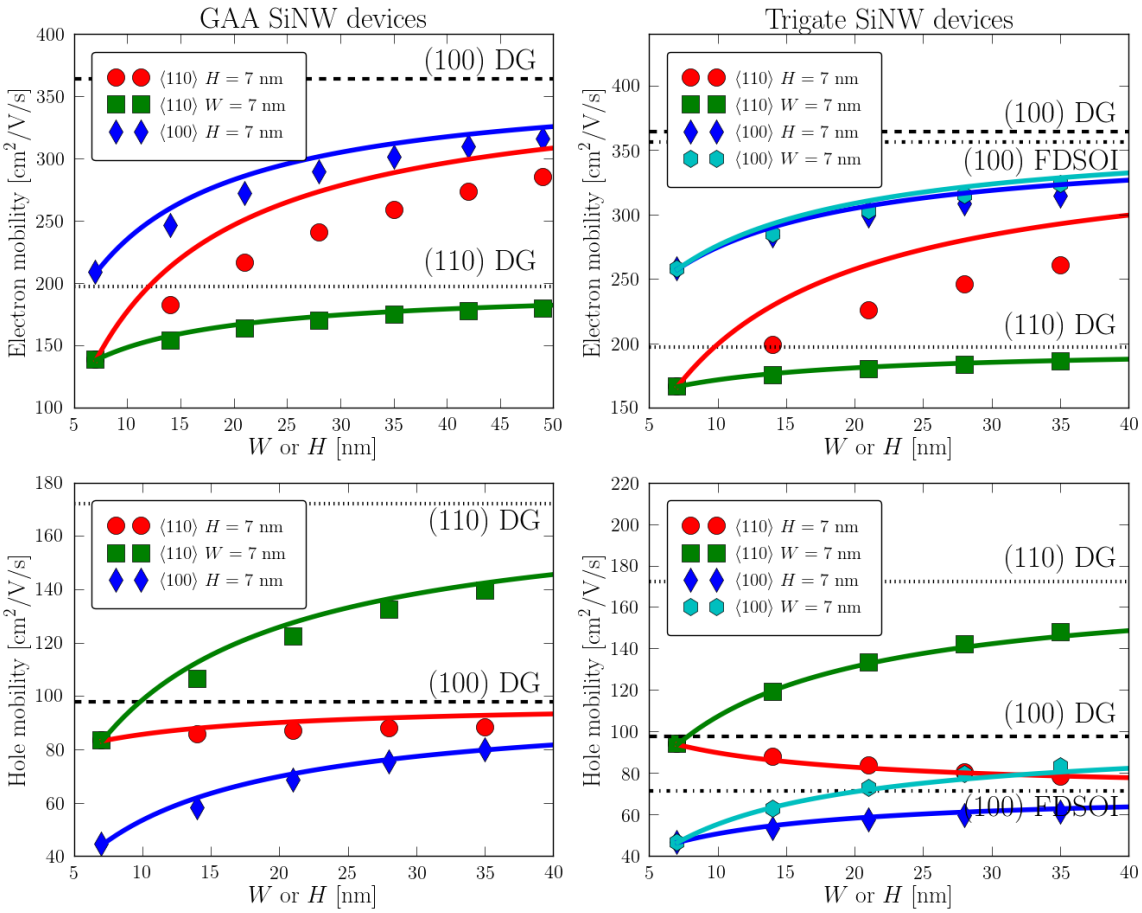

FIG. 1. (Color online) Phonon + SR limited electron (upper panel) and hole (lower panel) mobilities in rectangular ⟨100⟩ and ⟨110⟩ GAA (left panel) and Trigate (right panel) SiNW devices as a function of width (W) or height (H) at carrier density $n = 10^{13}$ cm^{-2}. The symbols are the NEGF results. The dashed lines, dashed dotted lines, dotted lines are the NEGF reference mobilities in planar (100) DG, (100) FDSOI and (110) DG devices, respectively. The solid lines are the interpolations from square NW devices to the limiting devices using our simple interpolation model (Eqs. 2 and 3).

On-Insulator (SOI) layer. It is lying on a 25 nm thick buried oxide (BOX), followed by a n-doped substrate (donor concentration $N_d = 10^{18}$ cm^{-3}) for n-NWFETs and p-doped substrate (acceptor concentration $N_p = 10^{18}$ cm^{-3}) for p-NWFETs, respectively. We consider both ⟨100⟩ [with {001} facets] and ⟨110⟩ [with horizontal (001) and vertical ($1\bar{1}0$) facets] transport orientations. The gate-stack is made of 0.6 nm of SiO_2 (dielectric constant $\epsilon = 3.9$) and 2.4 nm of HfO_2 ($\epsilon = 20$).

The structural scattering mechanisms, SR and RCS (charges trapped at the SiO_2/HfO_2 interface), are taken into account in our calculations. They are explicitly described in the geometries. For SR, we use a Gaussian auto-correlation function model with correlation length $\Lambda_{SR} = 1.0$ nm and rms fluctuation $\Delta_{SR} = 0.45$ nm. It is found that the sign of the RCS charges has nearly no effect on the carrier mobility in a given device. They are therefore assumed to be positive in our calculations, with a density $n_{RCS} = 2 \times 10^{13}$ cm^{-2}.

The current is computed in a self-consistent NEGF framework, on top of the effective mass approximation (EMA) or two bands $\mathbf{k} \cdot \mathbf{p}$ model for electrons and on top of the three bands $\mathbf{k} \cdot \mathbf{p}$ model for holes. The NEGF equations are solved using a fully coupled mode space approach (80 modes to 420 modes depending on the device cross section and on the band structure model) on a finite differences grid with step 2 Å. Carrier-phonon scattering is treated by using the deformation potential theory and self-consistent Born approximation with local self-energies. For electron-phonon scattering, we consider the intra-valley acoustic phonon scattering (with deformation potential $D_{ac} = 14.6$ eV) and 3 f-type and 3

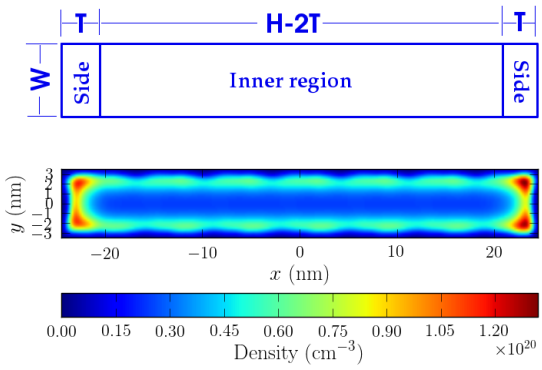

FIG. 2. (Color online) Contour plot of the electron charge density distribution (lower panel) in rectangular ⟨100⟩-oriented GAA SiNW device with $W = 7$ nm and $H = 49$ nm at electron density $n = 9.75 \times 10^{12}$ cm^{-2}. Upper panel: schematic representation of the partition of charge density distribution shown in the lower panel into two contributions, one from the "side channels" with thickness T, and one from the inner region with thickness $H - 2T$.

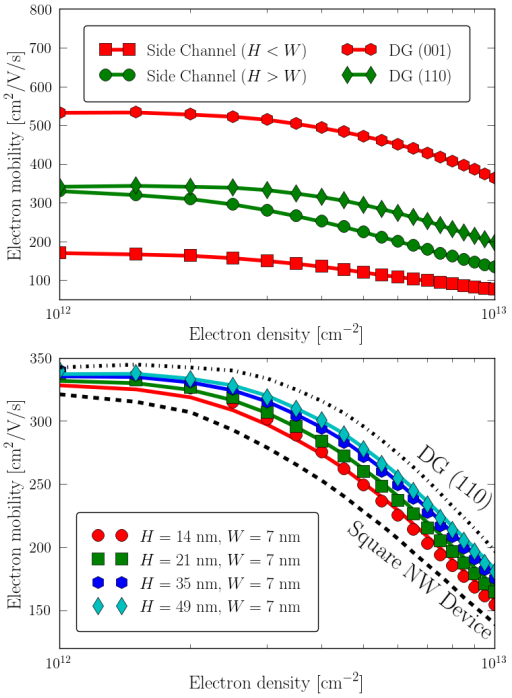

FIG. 3. (Color online) Upper panel: Electron mobility in the "side channels" extracted from the data for ⟨110⟩ GAA SiNWs with $W = 7$ nm or $H = 7$ nm by using $T = 3.5$ nm, and mobility computed in 7 nm-thick (100) and (110) DG devices. Lower panel: Mobility in ⟨110⟩ GAA SiNW with $W = 7$ nm as a function of electron density for different H. The solid lines represent the interpolations using our simple model [Eq. (3)]. The symbols and dotted lines represent the NEGF mobilities.

g-type processes of Ref. 27 for inter-valleys scattering. We use a diagonal hole-phonon interaction with one single acoustic deformation potential $D_{\rm ac} = 16.5$ eV and one single optical deformation potential $DK_{\rm opt} = 15$ eV/Å. More detailed information about the carrier-phonon self-energies and solution of the NEGF and Poisson equations can be found in the Appendix of Ref. 28.

The simulations are performed on fully gated undoped channels at small drain-source voltage ($V_{ds} = 20$ mV), as detailed in Ref. 28. Two methods are used for extracting the carrier mobility. One is the quasi-Fermi level analysis[29], in which the carrier mobility is obtained from the slope of the quasi-Fermi level along the channel. This method is computationally efficient and is approved to be accurate from moderate to strong inversion regime. However, it is often less accurate at low carrier densities. The other method is the numerical transmission line method[28], which extracts the carrier mobility from the linear variation of the total resistance R with respect to the channel length L. In order to limit variability, the same sample of disorder is repeated two or three times and the resistance is computed for each length. This method is free from contact resistance contamination and channel length misestimates. It thus allows a very accurate extraction of the carrier mobility at any given carrier density. However, this method is computationally more demanding since at least two calculations on "long" devices are required.

III. RESULTS AND DISCUSSION

A. Size dependent modulation of carrier mobilities in GAA and Trigate devices

In this section, we analyze the dependence of the electron and hole mobilities in rectangular GAA and Trigate SiNWs as a function of width W, height H, and orientation. For this purpose, we have computed the phonon + SR limited mobility using the NEGF methodology described above. The electron and hole band structures are described within the EMA and three bands $\mathbf{k} \cdot \mathbf{p}$ models, respectively. The mobilities are extracted from the quasi-Fermi level analysis on 30 nm long channels. We have considered devices with one fixed dimension W or $H = 7$ nm and the other dimension H or W ranging from 7 to 49 nm. The mobilities have also been computed for the planar limits: for GAA devices, H or $W = \infty$ corresponds to a planar double-gate (DG) device. For Trigate devices, $H = \infty$ also corresponds to a DG device and

$W = \infty$ corresponds to a planar FDSOI device.

The results are shown in Fig. 1 (symbols). We find that (*i*) $\langle 100 \rangle$ *n*-NWFETs perform better than their $\langle 110 \rangle$ counterparts, and (*ii*) $\langle 110 \rangle$ *n*-NWFETs with width $W > H$ show larger mobilities than $\langle 110 \rangle$ *n*-NWFETs with height $H > W$. This holds for both GAA and Trigate devices. The reasons can be attributed to the band structure effects[30]. In [100] SiNWs, the Δ valleys split into light ($m^* = 0.19\ m_0$) $\Delta_{y,z}$ valleys at the Γ point, and much heavier ($m^* = 0.92\ m_0$) Δ_x valleys at $k \neq 0$. Under strong inversion bias, the electron gas is confined at the surface of the SiNW by the electric field, mostly in the light Δ_y valleys on the lateral (010) facets, and mostly in the light Δ_z valleys on the top and bottom (001) facets. In [110] SiNWs, the Δ valleys split into light ($m^* = 0.19\ m_0$) Δ_z valleys at Γ point and heavier ($m^* = 0.55\ m_0$) $\Delta_{x,y}$ valley off Γ. Again, under strong inversion bias the electron gas is mostly confined in the light Δ_z valleys on the top and bottom (001) facets, but in the heavier $\Delta_{x,y}$ valleys on the lateral $(1\bar{1}0)$ facets. Therefore, wide $\langle 110 \rangle$ SiNWs with dominant (001) facets ($W > H$) perform better than tall $\langle 110 \rangle$ SiNWs with dominant $(1\bar{1}0)$ facets ($H > W$). Likewise, $\langle 100 \rangle$ NWs with only $\{001\}$ facets show better mobilities than $\langle 110 \rangle$ SiNWs with mixed facets.

Opposite trends are found for *p*-NWFETs. Tall $\langle 110 \rangle$ SiNWs ($H > W$) indeed perform better than wide $\langle 110 \rangle$ SiNWs ($W > H$), and $\langle 110 \rangle$ *p*-NWFETs always outperform their $\langle 100 \rangle$ counterparts. These trends can again be understood from the band structure arguments. Indeed, holes confined on $\{110\}$ facets tend to show lighter transport masses than holes confined on $\{001\}$ facets[31]; in square $\langle 110 \rangle$ SiNWs the highest valence subband has a clear light hole character and is well separated from the others, while in square $\langle 100 \rangle$ SiNWs the topmost valence bands are almost degenerate and heavy, which decreases carrier velocity and enhances inter-subband scattering[30].

It is found from Fig. 1 that H and W play the same role in $\langle 100 \rangle$ GAA devices since (010) and (001) facets are equivalent. Although the facets' nature remains the same for Trigate devices, H has a larger weight in the effective channel width $W_{\rm eff} = 2H + W$ than W. Tall [100] Trigate *n*-NWFETs with a larger $W_{\rm eff}$ therefore slightly outperform the wide [100] counterparts. The situation is reversed in [100] Trigate *p*-NWFETs. We also find that increasing NW cross section tends to enhance the carrier mobility. The only exception appears for $\langle 110 \rangle$ *p*-NWFETs with $W > H$, where an increase in the (100) facet area with lower hole mobility is actually detrimental to the device performance. When increasing H or W, the carrier mobility tends to the expected DG or FDSOI limit. However, the convergence can be rather slow, especially for electrons in $\langle 110 \rangle$ SiNWs with $W > H$.

B. A simple interpolation model

In order to understand the physics behind, we analyze the carrier density in the devices (Fig. 2). For simplicity but without loss of generality, we focus on GAA devices. As shown in Fig. 2, the electron density in the moderate to strong inversion regime peaks in four "corner channels" that tend to merge in two "side channels" when H or W is in the sub-10 nm range. The electron (e) or hole (h) mobility can then be written as,

$$\mu^{(e,h)} = \frac{n_{\rm in}^{(e,h)}}{n_{\rm in}^{(e,h)} + n_{\rm Side}^{(e,h)}} \mu_{\rm DG}^{(e,h)} + \frac{n_{\rm Side}^{(e,h)}}{n_{\rm in}^{(e,h)} + n_{\rm Side}^{(e,h)}} \mu_{\rm Side}^{(e,h)}\ , \quad (1)$$

where $n_{\rm in}$ and $n_{\rm Side}$ are the charge densities per unit length in the inner region and side channels (outer region) of Fig. 2, and $\mu_{\rm DG}$ is the mobility in the limiting DG device. The mobility $\mu_{\rm Side}$ in the side channels can be extracted from the data with a suitable thickness of side channel T at a given size [e.g., $T = 3.5$ nm for device with $W = 7$ nm and $H = 14$ nm when analyzing $H > W$ devices]. Eq. (1) turns out to give an excellent description of the mobility at all sizes and densities. $\mu_{\rm Side}$ depends on the carrier density and facet orientation. The extracted $\mu_{\rm Side}$ is shown in Fig. 3 (upper panel) for $\langle 110 \rangle$ GAA SiNW devices. It is, as expected, lower on $(1\bar{1}0)$ than on (001) facets, and lower than in the corresponding DG device due to lateral quantum confinement in the side channel and enhanced SR and phonon scattering. When increasing W or H, $n_{\rm in}$ increases linearly while $n_{\rm Side}$ remains nearly constant. However, even for W or $H \simeq 50$ nm, still over 20% of the total charge density remains in the "side channels" with much lower mobility. This explains the slow convergence of the mobility towards the planar limit.

To further simplify the model, we assume that charge accumulation in both inner and outer regions is ruled by simple electrostatics and is thus proportional to the surface area, e.g. $n_{\rm in} \simeq \alpha(W - 2T)$ and $n_{\rm Side} \simeq \alpha(H + 2T)$ when $W > H$. Then Eq. (1) turns into a simple interpolation formula between the mobility $\mu_{\rm SQ}$ of the square NW ($H = W$) and the mobility of the limiting DG device $\mu_{\rm DG}$, namely:

$$\mu^{(e,h)} \approx \frac{W - H}{W + H} \mu_{\rm DG}^{(e,h)} + \frac{2H}{W + H} \mu_{\rm SQ}^{(e,h)} \quad (2)$$

when $W > H$, and:

$$\mu^{(e,h)} \approx \frac{H - W}{W + H} \mu_{\rm DG}^{(e,h)} + \frac{2W}{W + H} \mu_{\rm SQ}^{(e,h)} \quad (3)$$

when $W < H$. For Trigate devices, $\mu_{\rm DG}$ in Eq. (2) has to be replaced by the mobility of the limiting FDSOI device $\mu_{\rm FDSOI}$. $\mu_{\rm SQ}$ then represents the mobility of square Trigate device. These equations well reproduce the NEGF results over a wide range of dimensions and carrier densities, as shown in Figs. 1 and 3 (lower panel), whatever the NW orientations.

TABLE I. Compiled fitting parameters α, β and γ in Eqs. (5) and (6) for phonon-limited (PH), SR-limited (SR) and RCS-limited (RCS) partial electron mobilities of [100] and [110]-oriented square GAA SiNW devices. μ^{ref}, in unit of cm^2/V/s, is the corresponding NEGF calculated partial mobility at reference density $N_{\rm ref} = 2 \times 10^{12}$ cm^{-2}. The units of α, β and γ are cm^2, cm^4 and unity, respectively.

	[100]							
	PH			SR			RCS	
Size (nm)	$\mu_{\rm PH}^{\rm ref}$	$\alpha^{\rm PH}$	$\beta^{\rm PH}$	$\mu_{\rm SR}^{\rm ref}$	$\alpha^{\rm SR}$	$\beta^{\rm SR}$	$\mu_{\rm RCS}^{\rm ref}$	γ
5	372	2.73E-14	-2.38E-28	9.53E2	-1.09E-14	3.21E-26	281	1.19
7	476	1.38E-14	2.90E-27	1.68E3	1.28E-13	4.45E-26	463	0.77
10	509	6.34E-14	1.98E-28	2.20E3	2.07E-12	6.05E-26	491	0.79
	[110]							
	PH			SR			RCS	
Size (nm)	$\mu_{\rm PH}^{\rm ref}$	$\alpha^{\rm PH}$	$\beta^{\rm PH}$	$\mu_{\rm SR}^{\rm ref}$	$\alpha^{\rm SR}$	$\beta^{\rm SR}$	$\mu_{\rm RCS}^{\rm ref}$	γ
5	417	1.83E-14	1.09E-27	6.48E2	9.29E-14	2.03E-26	317	1.08
7	459	4.62E-14	2.44E-28	1.24E3	2.29E-13	5.29E-26	486	0.70
10	452	4.48E-14	-4.74E-28	1.62E3	1.52E-12	6.08E-26	474	0.79

TABLE II. The same as in Table I but for hole partial mobilities.

	[100]							
	PH			SR			RCS	
Size (nm)	$\mu_{\rm PH}^{\rm ref}$	$\alpha^{\rm PH}$	$\beta^{\rm PH}$	$\mu_{\rm SR}^{\rm ref}$	$\alpha^{\rm SR}$	$\beta^{\rm SR}$	$\mu_{\rm RCS}^{\rm ref}$	γ
5	68	-2.63E-14	1.87E-27	102	7.24E-14	2.45E-27	203	1.38
7	88	7.42E-16	1.85E-27	304	2.44E-13	1.15E-27	458	0.76
10	100	3.58E-15	1.18E-27	749	2.88E-13	3.69E-26	506	0.63
	[110]							
	PH			SR			RCS	
Size (nm)	$\mu_{\rm PH}^{\rm ref}$	$\alpha^{\rm PH}$	$\beta^{\rm PH}$	$\mu_{\rm SR}^{\rm ref}$	$\alpha^{\rm SR}$	$\beta^{\rm SR}$	$\mu_{\rm RCS}^{\rm ref}$	γ
5	216	-2.51E-16	3.85E-27	336	2.77E-13	1.32E-26	310	1.06
7	213	-5.82E-16	3.06E-27	451	2.33E-13	5.29E-27	425	0.82
10	205	-4.44E-14	5.22E-27	682	2.65E-13	3.31E-26	585	0.57

C. Carrier mobilities in square nanowire and limiting thin film devices

The simple interpolation model described previously requires the carrier mobilities of square NW devices ($\mu_{\rm SQ}$) and of limiting thin film devices ($\mu_{\rm DG}$ or $\mu_{\rm FDSOI}$) as inputs. To provide these inputs for sub-10 nm devices, we first computed the reference partial mobilities for various elastic scattering mechanisms, such as SR and RCS. These partial mobilities are defined with respect to the phonon-limited mobility $\mu_{\rm PH}$ as

$$\mu_{\rm M}^{-1} = \mu_{\rm PH+M}^{-1} - \mu_{\rm PH}^{-1}, \tag{4}$$

where M denotes a given elastic mechanism (SR or RCS), and $\mu_{\rm PH+M}$ is the NEGF mobility computed by including phonons and the scattering mechanism M. The partial mobilities obtained in this way satisfy Matthiessen's rule for multiple mechanisms much better than the usual, direct single mechanism calculations[28]. For SR, the reference correlation length and rms SR fluctuation are chosen as $\Lambda_{\rm SR}^{\rm ref} = 1.0$ nm and $\Delta_{\rm SR}^{\rm ref} = 0.45$ nm, which are widely accepted values. For RCS, the reference density of RCS charges is $n_{\rm RCS}^{\rm ref} = 2 \times 10^{13}$ cm^{-2} . It is well known that the EMA tends to overestimate the electron mobility though it is computationally less expensive. In what follows, we therefore have employed a two bands $\mathbf{k} \cdot \mathbf{p}$ model for the electron band structure calculations in order to offer accurate results for possible comparisons with experiments. The carrier mobilities are extracted from the transmission line method.

By this way, we have computed $\mu_{\rm PH}$, $\mu_{\rm SR}$ and $\mu_{\rm RCS}$ as a function of carrier density for n-type and p-type, square Trigate and GAA SiNW devices and also for the limiting DG and FDSOI devices. Various NW sizes (e.g., $W = H = 5,\ 7,\ 10$ nm, respectively) and film thickness (e.g., $T = 5,\ 7,\ 10$ nm, respectively) in the sub-10 nm range are considered. Some general characteristics for phonon-limited mobility $\mu_{\rm PH}$ and SR limited mobility $\mu_{\rm SR}$ are found:
(i) Both $\mu_{\rm PH}$ and $\mu_{\rm SR}$ decrease as a function of carrier density. However, comparing to $\mu_{\rm PH}$, the decreasing in $\mu_{\rm SR}$ is much faster. This makes SR the dominant mechanism at high inversion density.
(ii) At low carrier density, $\mu_{\rm SR}$ actually decreases with reducing the cross sectional area or film thickness of the devices, whatever the gate architecture and transport orientation (cf. $\mu_{\rm SR}^{\rm ref}$ in Tables I – VII). So does $\mu_{\rm PH}$. The only exception is for [110] p-FETs where the hole mo-

TABLE III. The same as in Table I but for electron partial mobilities in double gate (DG) devices.

	[100]							
	PH			SR			RCS	
Thickness (nm)	$\mu_{\rm PH}^{\rm ref}$	$\alpha^{\rm PH}$	$\beta^{\rm PH}$	$\mu_{\rm SR}^{\rm ref}$	$\alpha^{\rm SR}$	$\beta^{\rm SR}$	$\mu_{\rm RCS}^{\rm ref}$	γ
5	517	3.90E-14	-6.27E-28	2.36E3	2.42E-13	9.56E-27	547	0.88
7	556	1.77E-14	8.94E-28	3.61E3	2.37E-13	4.43E-26	676	0.77
10	577	3.36E-14	4.98E-28	4.25E3	1.20E-12	1.24E-25	736	0.68
	[110]							
	PH			SR			RCS	
Thickness (nm)	$\mu_{\rm PH}^{\rm ref}$	$\alpha^{\rm PH}$	$\beta^{\rm PH}$	$\mu_{\rm SR}^{\rm ref}$	$\alpha^{\rm SR}$	$\beta^{\rm SR}$	$\mu_{\rm RCS}^{\rm ref}$	γ
5	378	-1.3E-14	1.4E-27	1.13E3	-3.7E-15	1.1E-26	524	1.06
7	436	1.6E-14	1.3E-27	2.61E3	1.7E-13	4.9E-26	677	0.72
10	441	4.6E-14	-8.3E-28	3.15E3	1.4E-12	1.9E-25	728	0.66

TABLE IV. The same as in Table I but for hole partial mobilities in double gate (DG) devices.

	[100]							
	PH			SR			RCS	
Thickness (nm)	$\mu_{\rm PH}^{\rm ref}$	$\alpha^{\rm PH}$	$\beta^{\rm PH}$	$\mu_{\rm SR}^{\rm ref}$	$\alpha^{\rm SR}$	$\beta^{\rm SR}$	$\mu_{\rm RCS}^{\rm ref}$	γ
5	115	-1.63E-14	9.53E-28	396	1.45E-15	9.17E-27	85	1.79
7	130	-1.69E-14	1.15E-27	957	1.10E-13	3.49E-26	158	1.49
10	146	-2.51E-14	3.59E-27	1.4E3	4.65E-13	7.23E-26	302	0.98
	[110]							
	PH			SR			RCS	
Thickness (nm)	$\mu_{\rm PH}^{\rm ref}$	$\alpha^{\rm PH}$	$\beta^{\rm PH}$	$\mu_{\rm SR}^{\rm ref}$	$\alpha^{\rm SR}$	$\beta^{\rm SR}$	$\mu_{\rm RCS}^{\rm ref}$	γ
5	337	2.80E-15	1.92E-27	1.18E3	3.86E-13	-2.01E-27	158	1.47
7	315	-2.60E-14	3.22E-27	1.53E3	5.62E-13	6.88E-27	216	1.22
10	302	-3.95E-14	3.92E-27	1.65E3	1.25E-12	-3.64E-27	271	1.02

bility is beneficial from the decrease in NW size or film thickness.

(*iii*) Equally sized Trigate and GAA devices show very similar $\mu_{\rm PH}$. And, so do their [100] DG and FDSOI counterparts with the same film thickness.

(*iv*) The dependence of $\mu_{\rm PH}$ or $\mu_{\rm SR}$ on carrier density is best modelled by the following function,

$$\mu_{\rm M} = \mu_{\rm M}^{\rm ref} \frac{1+\alpha_M N_{\rm ref} + \beta_{\rm M} N_{\rm ref}^2}{1+\alpha_{\rm M} N + \beta_M N^2}, \tag{5}$$

where "M" denotes "PH" or "SR", $\mu_{\rm M}^{\rm ref}$ is the "M"-limited mobility at a "reference" carrier density $N_{\rm ref}$. α and β are the fitting parameters determined by best reproducing the NEGF results. The compiled values for these parameters are tabulated in Tables I – VII.

RCS is known to be one of the important scattering mechanisms at low inversion density. It becomes increasingly more important (cf. $\mu_{\rm RCS}^{\rm ref}$ in Tables I – VII) when reducing the cross sectional area S or the film thickness T. $\mu_{\rm RCS}$ is found to increase exponentially as a function of carrier density due to the screening of the RCS electrostatic potential. The increase is more pronounced at smaller S or T. We find that the dependence of $\mu_{\rm RCS}$ on carrier density is best described by the following function,

$$\mu_{\rm RCS} = \mu_{\rm RCS}^{\rm ref} (\frac{N}{N_{\rm ref}})^{\gamma}, \tag{6}$$

where $\mu_{\rm RCS}^{\rm ref}$ is the RCS-limited mobility at a "reference" density $N_{\rm ref}$. γ is the only free parameter which is determined by best reproducing the NEGF results. Unlike $\mu_{\rm PH}$, $\mu_{\rm SR}$ and $\mu_{\rm RCS}$ are found to be quantitatively different in GAA and Trigate devices (or DG and FDSOI devices) (cf. Tables I – VII). This can be attributed to the differences of the interface area in these devices. Finally, we find that significant quantum confinement effects do not appear until the NW size or film thickness reaches the sub-5 nm range, whatever the gate architecture, transport orientation and scattering mechanism.

From these reference partial mobilities, one can then construct the total mobility. Since $\mu_{\rm SR} \propto \frac{1}{\Delta^2}$ [28,32] and $\mu_{\rm RCS} \propto \frac{1}{n_{\rm RCS}}$ [33,34], we can write the total mobility μ, including PH, SR and RCS, as[35]

$$\frac{1}{\mu} = \frac{1}{\mu_{\rm PH}} + (\frac{\Delta_{\rm SR}}{\Delta_{\rm SR}^{\rm ref}})^2 \frac{1}{\mu_{\rm SR}^{\rm ref}} + \frac{n_{\rm RCS}}{n_{\rm RCS}^{\rm ref}} \frac{1}{\mu_{\rm RCS}^{\rm ref}}, \tag{7}$$

where $\Delta_{\rm SR}$ and $n_{\rm RCS}$ are two free parameters which are determined by best reproducing the experiments. It should be noted that $\mu_{\rm SR}$ also depends on the correlation length $\Lambda_{\rm SR}$. However, it has been shown that different ($\Lambda_{\rm SR}$, $\Delta_{\rm SR}$) pairs can yield the same mobility curves[36] and one can not determine $\Lambda_{\rm SR}$ and $\Delta_{\rm SR}$ independently. Therefore, we keep $\Lambda_{\rm SR}$ = 1.0 nm and only fit $\Delta_{\rm SR}$ to the experiments.

TABLE V. The same as in Table I but for electron partial mobilities in square Trigate SiNW devices.

	[100]							
	PH			SR			RCS	
Size (nm)	$\mu_{\rm PH}^{\rm ref}$	$\alpha^{\rm PH}$	$\beta^{\rm PH}$	$\mu_{\rm SR}^{\rm ref}$	$\alpha^{\rm SR}$	$\beta^{\rm SR}$	$\mu_{\rm RCS}^{\rm ref}$	γ
5	378	2.90E-14	-6.58E-28	1.0E3	3.60E-14	2.45E-26	330	0.99
7	482	1.14E-14	1.93E-27	1.86E3	2.26E-13	3.10E-26	493	0.72
10	514	5.17E-14	3.21E-28	2.39E3	2.49E-12	2.43E-26	559	0.65
	[110]							
	PH			SR			RCS	
Size (nm)	$\mu_{\rm PH}^{\rm ref}$	$\alpha^{\rm PH}$	$\beta^{\rm PH}$	$\mu_{\rm SR}^{\rm ref}$	$\alpha^{\rm SR}$	$\beta^{\rm SR}$	$\mu_{\rm RCS}^{\rm ref}$	γ
5	425	1.46E-14	8.94E-28	7.03E2	9.66E-14	1.56E-26	411	0.91
7	467	4.13E-14	9.01E-29	1.45E3	2.66E-13	4.86E-26	465	0.73
10	452	4.11E-14	-6.86E-28	1.80E3	1.70E-12	3.66E-26	589	0.61

TABLE VI. The same as in Table I but for hole partial mobilities in square Trigate SiNW devices.

	[100]							
	PH			SR			RCS	
Size (nm)	$\mu_{\rm PH}^{\rm ref}$	$\alpha^{\rm PH}$	$\beta^{\rm PH}$	$\mu_{\rm SR}^{\rm ref}$	$\alpha^{\rm SR}$	$\beta^{\rm SR}$	$\mu_{\rm RCS}^{\rm ref}$	γ
5	67	-1.95E-14	1.18E-27	107	5.17E-14	2.72E-27	118	1.17
7	87	-6.82E-15	2.37E-27	356	3.04E-13	-1.60E-27	159	0.84
10	98	1.86E-14	2.53E-28	853	1.55E-12	-2.28E-26	309	0.69
	[110]							
	PH			SR			RCS	
Size (nm)	$\mu_{\rm PH}^{\rm ref}$	$\alpha^{\rm PH}$	$\beta^{\rm PH}$	$\mu_{\rm SR}^{\rm ref}$	$\alpha^{\rm SR}$	$\beta^{\rm SR}$	$\mu_{\rm RCS}^{\rm ref}$	γ
5	219	-3.85E-16	2.54E-27	369	2.19E-13	1.21E-26	186	0.97
7	211	-3.59E-14	5.12E-27	501	3.28E-13	-5.23E-27	207	0.94
10	205	-3.24E-14	3.38E-27	722	3.73E-13	1.52E-26	229	0.85

D. Comparison with experimental data

To check the validity of our interpolation model and above strategy, we compare with experimental data on rectangular Trigate devices with $H = 11$ nm fabricated at CEA/LETI[37]. The equivalent oxide thickness (EOT) of high-k/metal gate stake is approximately 1.3 nm. The fitting parameters in Eq. (7) are optimized to reproduce both the carrier density dependent experimental mobility data of [110] n-type square Trigate device (e.g., $W = 13$ nm) and the experimental mobility data of [100] n-type FDSOI with film thickness $T = 11$ nm. In this procedure, we have used the previously computed partial mobilities of square Trigate devices with size 10 nm and the mobilities of FDSOI devices with film thickness 10 nm. Since quantum confinement effects become significant only in sub-5 nm devices, the errors caused by slight size mismatch between experimental and simulated devices should be marginal. The optimal values for $\Delta_{\rm SR}$ and $n_{\rm RCS}$ are,

$$\Delta_{\rm SR} = 0.43 \text{ nm},$$
$$n_{\rm RCS} = 1.42 \times 10^{13} \text{ cm}^{-2}. \quad (8)$$

With this single set of parameters and with the partial mobilities models compiled in Tables V-VII, Eq. (7) reproduces not only the experimental electron and hole mobilites of [110]-oriented square Trigate NW and thin film (FDSOI) devices but also the corresponding experimental data of [100]-oriented counterparts. Inputting these mobilities into the previously developed interpolation model (Eq. (2)), one can obtain the carrier mobility of rectangular Trigate device with any width ($W > H$) and at any carrier density. The interpolation with respect to NW width of [110]-oriented Trigate devices at a high inversion density is shown in Fig. 4. An excellent agreement between interpolations and experiments is obtained. Similar agreement has also been achieved for the carrier mobilities of [100]-oriented Trigate devices as a function of NW width at the same carrier density. These agreement therefore reinforces our deembedding strategy and also more importantly the interpolation model.

IV. CONCLUSIONS

We have performed quantum calculations on the carrier mobilities of n-type and p-type, gate-all-around and Trigate SiNW devices using a fully coupled mode-space non-equilibrium Green's Functions approach. We find that the carrier mobility improves with increasing the effective channel width $W_{\rm eff}$. The only exception is for p-type [110] NW and thin film devices. Enhancing the effective channel width turns out to degrade the device performance. Increasing nanowire height or width results

TABLE VII. The same as in Table I but for electron and hole partial mobilities in (100)-FDSOI devices.

	Electron							
	PH			SR			RCS	
Thickness (nm)	$\mu_{\rm PH}^{\rm ref}$	$\alpha^{\rm PH}$	$\beta^{\rm PH}$	$\mu_{\rm SR}^{\rm ref}$	$\alpha^{\rm SR}$	$\beta^{\rm SR}$	$\mu_{\rm RCS}^{\rm ref}$	γ
5	532	2.83E-14	5.69E-28	2.18E3	4.74E-14	4.29E-26	628	0.77
7	554	2.33E-14	9.76E-28	2.94E3	2.45E-13	6.50E-26	750	0.67
10	570	3.43E-14	3.12E-28	3.46E3	3.42E-13	1.00E-25	852	0.59
	Hole							
	PH			SR			RCS	
Thickness (nm)	$\mu_{\rm PH}^{\rm ref}$	$\alpha^{\rm PH}$	$\beta^{\rm PH}$	$\mu_{\rm SR}^{\rm ref}$	$\alpha^{\rm SR}$	$\beta^{\rm SR}$	$\mu_{\rm RCS}^{\rm ref}$	γ
5	116	-3.65E-17	1.15E-27	366	-1.21E-14	1.76E-26	151	1.32
7	128	1.54E-14	4.24E-28	895	3.28E-16	6.57E-26	221	1.05
10	136	3.45E-14	-8.32E-28	1.3E3	1.27E-13	1.43E-25	309	0.84

in a gradual convergence of carrier mobility towards the double gate or FDSOI limit. However, this convergence procedure can be rather slow under certain condition. This is attributed to the formation of "side channels" from the merging of neighboring corner channels, which holds very low mobility. Their contribution remains significant even in rectangular devices with large width or height up to 50 nm.

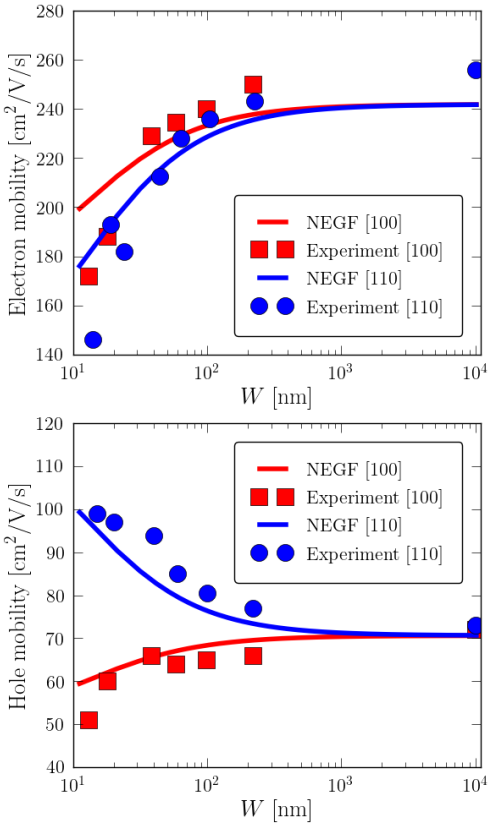

FIG. 4. (Color online) Electron (upper panel) and hole (lower panel) mobilities as a function of W of rectangular Trigate SiNW devices at carrier density $n = 10^{13}$ cm^{-2}. The symbols are the experimental data, while the solid curves are the interpolations using our model on top of constructed mobilities for square SiNW devices and DG devices using Eq. (7). Here, the NW height $H = 11$ nm.

On top of the numerical results, we have derived a simple but effective interpolation model for the size-dependent carrier mobilities in rectangular SiNW devices. As inputs, the mobilities of square SiNW devices and of the limiting thin film devices are required. We have developed a strategy to construct these mobilities by combining contributions from phonons, SR and RCS of reference devices in a way consistent with Matthiessen's rule. However, SR and RCS contributions in real devices can be different from the chosen reference ones. Weighting factors are therefore added and they are treated as adjustable parameters to best reproducing the experimental data. We have therefore further computed the phonons-, SR- and RCS-limited partial mobilities of the targeting devices with various sizes or thickness in sub-10 nm range. The characteristics of these partial mobilities are discussed and empirical functions are developed to describe their carrier density dependence. Finally, the derived mobility interpolation model and the strategy of construing its inputs have been validated by comparing with in-house experiments. The results might be useful for compact modelling of SiNW transistors.

ACKNOWLEDGMENT

This work was supported by the French National Research Agency (ANR) project Noodles, and partly supported by the European Union Horizon 2020 research and innovation program under grant agreement No. 688101 SUPERAID7. The calculations were run on the TGCC/Curie machine thanks to allocations from GENCI and PRACE.

[1] M. Bohr, in *IEDM Tech. Dig.* (2011) pp. 1–6.
[2] K. J. Kuhn, IEEE Trans. Electron Device **59**, 1813 (2012).

[3]J.-P. Colinge, *FinFETs and Other Multi-Gate Transistors* (Springer US, 2008).
[4]M. C. McAlpine, R. S. Friedman, S. Jin, K.-h. Lin, W. U. Wang, and C. M. Lieber, Nano Lett. **3**, 1531 (2003).
[5]J. Goldberger, A. I. Hochbaum, R. Fan, and P. Yang, Nano Lett. **6**, 973 (2006).
[6]X. Liu, Y.-Z. Long, L. Liao, X. Duan, and Z. Fan, ACS Nano **6**, 1888 (2012).
[7]O. Gunawan, L. Sekaric, A. Majumdar, M. Rooks, J. Appenzeller, J. W. Sleight, S. Guha, and W. Haensch, Nano Lett. **8**, 1566 (2008).
[8]J. Chen, T. Saraya, K. Miyaji, K. Shimizu, and T. Hiramoto, Jpn. J. Appl. Phys. **48**, 011205 (2009).
[9]J. Chen, T. Saraya, and T. Hiramoto, IEEE Electron Device Lett. **30**, 1203 (2009).
[10]L. Sekaric, O. Gunawan, A. Majumdar, X. H. Liu, D. Weinstein, and J. W. Sleight, Appl. Phys. Lett. **95**, 023113 (2009).
[11]P. Hashemi, J. T. Teherani, and J. L. Hoyt, in *IEDM Tech. Dig.* (2010) pp. 34.5.1–34.5.4.
[12]K. Mao, T. Saraya, and T. Hiramoto, Jpn. J. Appl. Phys. **52**, 04CC11 (2013).
[13]M. Luisier and G. Klimeck, Phys. Rev. B **80**, 155430 (2009).
[14]S. Kim, M. Luisier, A. Paul, T. B. Boykin, and G. Klimeck, IEEE Trans. Electron Device **58**, 1371 (2011).
[15]H. E. Jung and M. Shin, IEEE Trans. Electron Device **60**, 1861 (2013).
[16]N. Neophytou and H. Kosina, Nano Lett. **10**, 4913 (2010).
[17]M. Aldegunde, A. Martinez, and J. R. Barker, J. Appl. Phys. **113**, 014501 (2013).
[18]Y.-M. Niquet, C. Delerue, and C. Krzeminski, Nano Lett. **12**, 3545 (2012).
[19]I. Tienda-Luna, J. Roldn, F. Ruiz, C. Blanque, and F. Gamiz, Solid-State Electron. **90**, 18 (2013).
[20]R. Rhyner and M. Luisier, Phys. Rev. B **89**, 235311 (Jun 2014).
[21]R. Granzner, V. M. Polyakov, C. Schippel, and F. Schwierz, IEEE Trans. Electron Device **61**, 3601 (2014).
[22]H. Ryu, Nanoscale Res. Lett. **11**, 1 (2016).
[23]E. B. Ramayya, D. Vasileska, S. M. Goodnick, and I. Knezevic, IEEE Trans. Nanotechnol. **6**, 113 (2007).
[24]M. D. Michielis, D. Esseni, P. Palestri, and L. Selmi, IEEE Trans. Electron Device **56**, 2081 (2009).
[25]A. K. Buin, A. Verma, and M. P. Anantram, J. Appl. Phys. **104** (2008).
[26]J. W. Ma, W. J. Lee, J. M. Bae, K. S. Jeong, S. H. Oh, J. H. Kim, S.-H. Kim, J.-H. Seo, J.-P. Ahn, H. Kim, and M.-H. Cho, Nano Lett. **15**, 7204 (2015).
[27]C. Jacoboni and L. Reggiani, Rev. Mod. Phys. **55**, 645 (Jul 1983).
[28]Y.-M. Niquet, V.-H. Nguyen, F. Triozon, I. Duchemin, O. Nier, and D. Rideau, J. Appl. Phys. **115**, 054512 (2014).
[29]L. Bourdet, J. Li, J. Pelloux-Prayer, F. Triozon, M. Casse, S. Barraud, S. Martinie, D. Rideau, and Y.-M. Niquet, J. Appl. Phys. **119**, 084503 (2016).
[30]Y. M. Niquet, C. Delerue, and D. Rideau, in *2012 13th International Conference on Ultimate Integration on Silicon (ULIS)* (2012) pp. 49–52.
[31]P. Packan, S. Cea, H. Deshpande, T. Ghani, M. Giles, O. Golonzka, M. Hattendorf, R. Kotlyar, K. Kuhn, A. Murthy, P. Ranade, L. Shifren, C. Weber, and K. Zawadzki, in *IEDM Tech. Dig.* (2008) pp. 1–4.
[32]S. M. Goodnick, D. K. Ferry, C. W. Wilmsen, Z. Liliental, D. Fathy, and O. L. Krivanek, Phys. Rev. B **32**, 8171 (1985).
[33]F. Gamiz, J. B. Roldan, J. E. Carceller, and P. Cartujo, Appl. Phys. Lett. **82**, 3251 (2003).
[34]P. Toniutti, P. Palestri, D. Esseni, F. Driussi, M. De Michielis, and L. Selmi, J. Appl. Phys. **112**, 034502 (2012).
[35]V. H. Nguyen, Y. M. Niquet, F. Triozon, I. Duchemin, O. Nier, and D. Rideau, IEEE Trans. Electron Device **61**, 3096 (2014).
[36]A. Pirovano, A. L. Lacaita, G. Ghidini, and G. Tallarida, IEEE Electron Device Lett. **21**, 34 (2000).
[37]S. Barraud, M. Casse, L. Gaben, Y. Pelloux-Prayer, Z. Zeng, F. Triozon, and Y. M. Niquet , Submitted for publication.